

Self-consistent three-dimensional model of dust particle transport and formation of Coulomb crystals in plasma processing reactors

Vivek Vyas^{a)}

Department of Materials Science and Engineering, University of Illinois, Urbana, Illinois 61801

Gregory A. Hebner^{b)}

Sandia National Laboratories, Albuquerque, New Mexico 87185-1423

Mark J. Kushner^{c)}

Department of Electrical and Computer Engineering, University of Illinois, Urbana, Illinois 61801

(Received 24 June 2002; accepted 30 August 2002)

Dust particle transport in low-temperature plasmas has received considerable attention due to the desire to minimize contamination of wafers during plasma processing of microelectronic devices and for their use to study nonideal plasmas. Dust particles in radio frequency discharges form Coulomb crystals and display collective behavior under select conditions. In this article, we discuss results from a self-consistent three-dimensional model for dust particle transport in plasma processing reactors. The consequences of varying the bias voltage of the capacitively coupled discharge, plasma density, particle diameter, and the number of particles on the propensity for Coulomb crystal formation in argon plasmas will be discussed. We found that a single one-layer lattice spontaneously breaks up into separate lattices as the substrate bias is increased due to a redistribution of plasma forces. At high substrate biases, a void occurs in the plasma crystal which tends to close upon addition of electronegative gases such as O₂ and Cl₂ to argon. The interparticle spacing in the lattice depends on the number of particles in the lattice due to gravitational compressive forces; and on the plasma density due to the change in shielding length. © 2002 American Institute of Physics. [DOI: 10.1063/1.1516865]

I. INTRODUCTION

Dust particle transport in partially ionized plasmas has been the focus of many recent investigations as a consequence of concern over particle contamination of wafers during plasma processing of microelectronic devices and for the use of particles to study non-ideal plasmas.^{1–10} Particles in plasmas charge negatively to balance the flux of electrons and ions to their surfaces. As a consequence, the transport of these particles is governed by both mechanical (fluid drag, thermophoresis, gravity) and electrical (ion drag, electrostatic) forces. Ion drag forces accelerate particles in the direction of the net ion momentum, usually towards boundaries. Electrostatic forces accelerate particles opposite the electric field. Particle trapping in plasmas typically occurs where these forces balance.

Particle–particle Coulomb interactions become important when the dust density is high enough that interparticle spacing approaches the plasma shielding length, such as within a trapping site. Particles interact through Debye shielded Coulomb forces. If the density of the particles reaches a critical level, particles begin to display collective behavior; a system typically referred to as a Coulomb solid or liquid. Evidence of such behavior has been seen in a variety of laboratory discharges.^{2–6} For example, Melzer,

Homann, and Piel⁸ produced Coulomb crystals of 9.4 μm particles in rf discharges sustained in He. They found that reducing the gas pressure or increasing the discharge power resulted in melting of the crystal. These transitions were attributed to an increase in the effective temperature of the particles. The interparticle distance in the lattice increases with decreasing discharge power because the Debye shielding length is larger due to lower plasma density.⁷ A larger separation is typically observed between larger particles due to their stronger repulsive forces, as the amount of charge on a particle increases with its diameter.³ Recently Hebner *et al.*⁶ investigated particle interactions directly from the lateral compression of two-dimensional plasma dust crystals confined in a parabolic potential well in a rf discharge. They found that the interparticle separation typically decreased with increasing number of particles due to an increase in compressive forces in the parabolic well, and that interparticle spacing increased with increasing radial position in the well due to lessening of these compressive forces.

Dust particles may also arrange in vertically aligned structures or “strings.” Positive ions flowing past and focusing beyond negative charged particles, a phenomenon known as “ion streaming,” generate wake fields of positive space charge. The positive space charge in the wake field below trapped particles can be sufficiently large that particles at lower heights are attracted to that location, thereby producing vertical correlations between particles. Recently Joyce *et al.*¹⁰ developed a model which combines properties of molecular dynamics simulations to address the short-range por-

^{a)}Electronic mail: vvyas@uiuc.edu

^{b)}Electronic mail: gahebne@sandia.gov

^{c)}Author to whom correspondence should be addressed; electronic mail: mjk@uiuc.edu

tion of the shielded potential with a particle-in-cell methodology for the long-range part. They observed that particles formed hexagonal lattices when there was no ion streaming and “strings” in the presence of streaming.

Experiments have also demonstrated the formation of stable dust-free regions or “voids” in Coulomb crystals. Samsonov and Goree¹¹ observed that the void has a sharp boundary with the surrounding dusty plasma and the electron density and ionization rate were enhanced in the void. This enhanced ionization rate leads to electric fields which are directed outward from the void’s center. There is then a balance of an inward electrostatic force and an outward ion drag force which produces the void. Oscillations of charged dust particles trapped in a low temperature plasma sheath have also been observed. Recent studies have revealed vertical oscillations of single particles^{12,13} as well as horizontal dust lattice waves.^{14–16} The study of these oscillations is a useful tool for evaluating the particle charge and interparticle Coulomb coupling parameter.

In this article, we discuss results from a self-consistent three-dimensional model for dust particle transport in plasma processing reactors. A dust particle transport model was integrated into a plasma equipment model to facilitate this study. We discuss the effect of varying the bias voltage of a capacitively coupled discharge, gas chemistries, particle diameter, and the number of particles on the propensity for crystal formation. We found that higher radial ion drag forces at higher substrate biases produce voids in the plasma crystal. The presence of negative ions in the plasma causes closure of the void. The model will be described in Sec. II, followed by a discussion of our parametric results in Secs. III and IV. Concluding remarks are in Sec. V.

II. DESCRIPTION OF THE MODEL

The integrated dust transport module and the plasma kinetics models are based on the previously described Hybrid Plasma Equipment Model (HPEM)^{17,18} and the Dust Transport Simulation (DTS).¹⁹ When used separately, the HPEM produces plasma parameters (ion and neutral fluxes, electron, ion and neutral temperatures, and electric fields) which are used, in a postprocessing manner, in the DTS to calculate forces on the dust particles and their trajectories. As a result of the post processing nature of the DTS, feedback to the plasma resulting from the charge and the surface chemistry of the particles was not previously included. That inconsistency is corrected in this work.

The HPEM is a comprehensive simulator of low-pressure plasma reactors, as described in detail in Refs. 17 and 18. The HPEM is a two- or three-dimensional simulation consisting of three main modules. In the electromagnetics module (EEM), antenna generated electromagnetic fields are obtained using a frequency domain solution of Maxwell’s equations. Magnetostatic fields are calculated in a companion module. These fields are used in the electron energy transport module (EETM) where electron impact source functions and transport coefficients are derived. Results from the EETM are transferred to the fluid-chemical kinetics module (FKM) to determine plasma source and sink terms. The

FKM solves continuity, momentum and energy equations for charged and neutral species and Poisson’s equation for the electric potential. The outputs of the FKM are then fed back to the EEM and EETM modules for updated computations. The process iterates until a converged solution is obtained. For the results discussed here, the following options in the HPEM were used. Since a rf capacitively coupled reactor is being addressed, only the EETM and FKM modules were used. The electron transport coefficients were obtained using the electron energy equation option of the EETM. Continuity, momentum and energy equations were solved for ions and neutral particles, while the drift-diffusion continuity equation was solved for electrons. Poisson’s equation was solved for the electrostatic potential using a semi-implicit technique.

The DTS is a three-dimensional model in which the trajectories of dust particles are integrated based on mechanical and electrical forces.¹⁹ The forces included in the model are ion drag, fluid drag, electrostatic, thermophoretic, Coulomb, self-diffusive, gravity, and Brownian motion. The particle’s electric potential is based on balancing the electron and ion currents to the particle. The ion flux to the particle is given by the orbital motion limited current, which in turn depends on the plasma density and the ion energy. The ion and electron currents to a particle are²⁰

$$I_I = \pi a^2 N_I q \sqrt{\frac{2E_I}{m_I}} \left(1 - \frac{q\Phi}{E_I} \right), \quad (1)$$

$$I_e = \pi a^2 N_e q \sqrt{\frac{8kT_e}{\pi m_e}} \exp\left(\frac{q\Phi}{kT_e}\right), \quad (2)$$

where a is the particle radius, T_e is the electron temperature, m_e is the electron mass, m_I is the ion mass, E_I is the ion energy, N_e is the electron density, N_I is the ion density, and Φ is the particle potential. The particle electrical floating potential is obtained by equating Eqs. (1) and (2), thereby requiring that the negative and positive currents to the particle are equal. Given Φ in this manner, the charge on the particle Q is given by^{21,22}

$$Q = C\Phi, C = 4\pi\epsilon_0 a \left(1 + \frac{a}{\lambda_L} \right), \quad (3)$$

where C is the capacitance of the dust particle and λ_L is the linearized Debye length. The shielding length of the plasma around a highly negatively charged dust particle produced by ions and electrons is obtained by linearizing the Poisson–Vlasov equation²⁰

$$\frac{1}{\lambda_L} = \sqrt{\frac{e^2}{\epsilon_0} \left(\frac{N_e}{kT_e} + \frac{N_I}{2E_I} \right)}. \quad (4)$$

Ion drag forces result from the net transfer of momentum to dust particles. The ion-dust momentum transfer cross section is provided by the semianalytic formula by Kilgore *et al.*²¹

$$\sigma = b^2 c_1 \ln \left[1 + \frac{c_2}{(b/\lambda_L)^2} \right], \quad b = \frac{Q^2}{4\pi\epsilon_0 E_I}, \quad (5)$$

where $c_1 = 0.9369$ and $c_2 = 61.32$ are semiempirical values. Khrapak *et al.*²² have recently derived an expression for the

ion drag force from first principles accounting for both orbital motion and collisional impact. Their expression agrees well with the numerical calculations of Kilgore *et al.*²¹ In the same vein, a molecular dynamics simulation of ion-dust particle interaction also yields essentially the same cross section,²³ and so the computationally less expensive method of Eq. (5) is used.

The Coulomb repulsive force between particles is based on the particle's shielded plasma potential, using the Debye-Huckel form

$$\Phi(r) = \Phi_0 \frac{a}{r} \exp\left[-\frac{(r-a)}{\lambda_L}\right]. \quad (6)$$

The interparticle Coulomb force between particles at locations \mathbf{r}_1 and \mathbf{r}_2 separated by distance $R = |\mathbf{r}_1 - \mathbf{r}_2|$ is then

$$\mathbf{F}(\mathbf{r}_1, \mathbf{r}_2) = \frac{Q_1 Q_2}{4\pi\epsilon_0} \frac{1}{R} \left(\frac{1}{R} + \frac{1}{\lambda_L}\right) \exp\left[-\frac{R - \left(\frac{a_1 + a_2}{2}\right)}{\lambda_L}\right] \frac{\mathbf{r}}{R}. \quad (7)$$

Trajectories of dust particles under the influence of these forces are simultaneously integrated using a second order Runge-Kutta technique. When considering interparticle forces, the calculation time required to account for the interaction of all pairs of pseudoparticles scales as N^2 (where N is the number of pseudoparticles), which can lead to lengthy computational times when thousands of pseudoparticles are used in the DTS. For computational speedup, interparticle forces are included only if the particles are within a specified distance of each other. This distance was determined by parameterizing the model. There is little qualitative difference in the results for interacting distances greater than $3\lambda_L$. Hence the maximum interaction distance was set to $5\lambda_L$ in order to include sufficient interactions with particles while avoiding unnecessarily large computational times.

In the integrated HPEM-DTS model, dust particles are introduced into the reactor after plasma properties (e.g., densities of charged and neutral species) computed by the HPEM have reached a steady state. At that time, after each iteration through the modules of the HPEM, electric fields, neutral and charged particle fluxes and densities and temperature gradients are exported to the DTS module. These quantities are then used to compute forces on the dust particles and integrate their trajectories. During execution of the DTS (typically for a few to 10s of milliseconds which is large compared to the rf period of 100 ns) the plasma properties obtained from the HPEM are held constant. At the end of a call to the DTS, dust particle densities and their charge state are returned to the HPEM. The locations of the dust particles are binned on the same numerical mesh as used in the HPEM and the densities are distributed on the mesh using finite sized particle techniques. The dust densities and their charges are then used in the solution of Poisson's equation, and in computing electron and ion transport. Dust densities and charges are held constant during the following iteration through the HPEM. The time spent in the DTS, and the time spent in the HPEM between calls to the DTS, were

empirically chosen to be small enough so that holding properties constant in this manner is an acceptable approximation.

Dust particles interact with other plasma species in the HPEM through their charge density which, when included in solution of Poisson's equation, perturbs the electric potential. They also interact by providing surfaces internal to the plasma upon which heterogeneous chemistry can occur, including recombination of charged particles. Particles are also sources of momentum loss for electrons and ions through collisions. The electron-dust collection cross section included in the EETM for electron energy ϵ is²⁴

$$\sigma_{\text{col}}(\epsilon) = \pi a^2 \left(1 - \frac{e\Phi}{\epsilon}\right), \quad (8)$$

for electron energies greater than $|e\Phi|$. The electron-dust momentum transfer cross section was evaluated from standard Coulomb scattering theory²⁴

$$\sigma_m(\epsilon) = 4\pi b_0^2 \ln\left[1 + \left(\frac{\lambda_L}{b_0}\right)^2\right]^{1/2}, \quad (9)$$

where b_0 is the scattering parameter for 90° collisions. The positive ion flux to the particles was forced to be the same as the cycle-average loss of electrons to the particles.

To quantify the character of dust particle clouds in our plasmas, we utilized two metrics; the Coulomb coupling parameter Γ and the pair correlation function (PCF), $g(r)$. To account for the screened charge on the dust particles due to ions, the Coulomb coupling parameter for a collection of N particles is

$$\Gamma = \frac{1}{N} \sum_{i=1}^N \Gamma_i, \quad \Gamma_i = \frac{\frac{Q_i}{4\pi\epsilon_0} \sum_j \frac{Q_j}{R_{ij}} \exp\left(-\frac{R_{ij}-a}{\lambda_L}\right)}{\frac{3}{2}kT_{\text{eff}}}, \quad (10)$$

where T_{eff} is the effective temperature of the particle and R_{ij} is the separation between particles. The effective temperature encompasses both thermal and directed energy, $3/2kT_{\text{eff}} = 3/2kT + 1/2mv^2$. Neglecting fluid drag effects, particles can convert a large fraction of their directed energy into randomized thermal energy due to Coulomb collisions with other particles. Large values of Γ ($>10-100$ s) denote a system which is dominated by interparticle forces, and so can be classified as a Coulomb fluid ($\Gamma \approx 1-10$ s) or a Coulomb solid ($\Gamma \approx 100$ s).

To examine the phases of the structures that form (solid versus liquid), the PCF is used. $g(r)$ is the probability of finding two particles separated by a distance r , as compared to that for an unstructured random distribution of particles. The PCF is calculated using the method described by Quinn *et al.*²⁵ A particle is chosen as the center point or test particle. The remaining particles in a specified region are then binned according to their distance from the test particle. These particle counts are then divided by the annular area defined by their distance from the test particle and are normalized by the resulting average particle density. This procedure is repeated using all the particles in the region as test particles and the

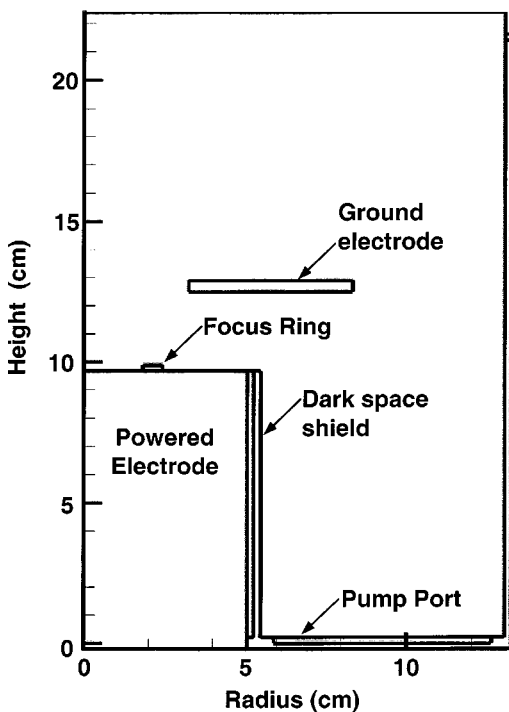


FIG. 1. Schematic of the modified GEC reference cell used in the simulations. The lower electrode is powered. An annular plate replaces the upper electrode. A metal washer placed on the lower electrode acts as a focus ring.

results averaged. Successive peaks in $g(r)$ at small r correspond, respectively, to first, second, and increasing nearest neighbors.

III. CHARACTERISTICS OF COULOMB FLUIDS AND SOLIDS IN rf DISCHARGES

The model reactor is a modified GEC reference cell schematically shown in Fig. 1. The lower electrode is powered at 10 MHz. An annular plate replaced the upper electrode so that, experimentally, particles can be observed from the top of the reactor.⁶ A metal washer placed on the lower electrode acts as a focus ring to warp the electric potential into a well to confine the dust particles. The plasma was sustained in argon at 95 mTorr with a flow rate of 300 sccm, which is exhausted through the pump port surrounding the lower electrode. The substrate bias was varied from 125 to 250 V. (Substrate bias refers to the amplitude of the rf voltage.) Dust particles of mass density 2.33 g cm^{-3} akin to that of amorphous silicon were initially randomly distributed between the electrodes. Their trajectories were integrated for approximately 8 s until they settled into a quasistable geometric configuration.

The electron density, electron temperature, and the time averaged plasma potential for a substrate bias of 150 V are shown in Fig. 2. The peak Ar^+ density is $1.2 \times 10^{10} \text{ cm}^{-3}$ and peak plasma potential is 95 V, including a -7 V dc bias on the substrate. The plasma penetrates through the annular grounded electrode into the upper chamber. The plasma potential is largely flat in the body of the plasma. Sheaths surround the annulus and there are large ambipolar electric fields in the periphery of the reactor. The ion density and

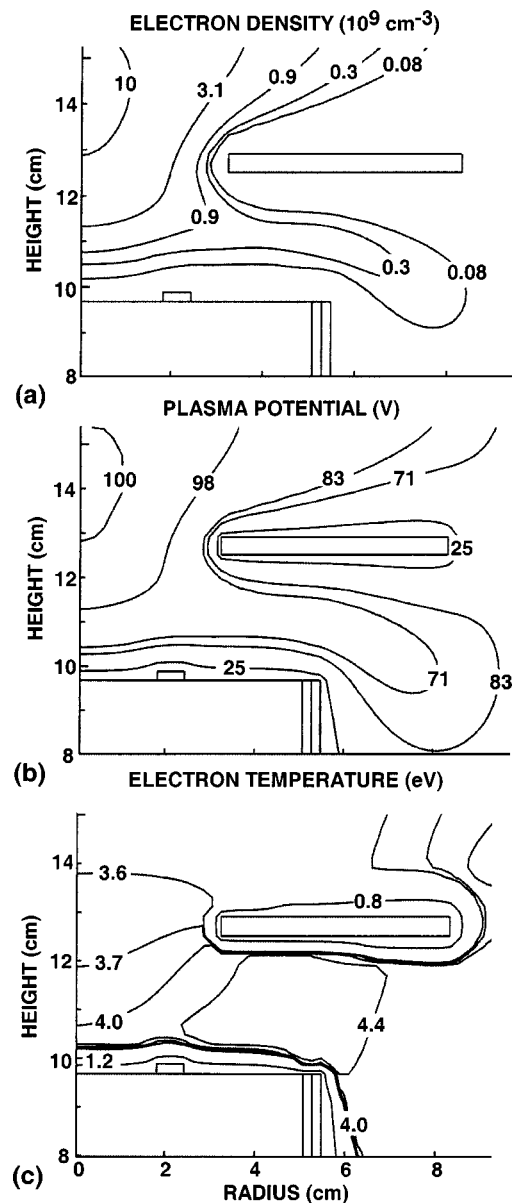


FIG. 2. Plasma properties in an Ar discharge (95 mTorr, 300 sccm) for a substrate bias for 150 V. (a) Electron density. (b) Plasma potential. (c) Electron temperature.

plasma potential are conformal to the focus ring forming a potential well in which the particles are trapped. Trapped particles are usually confined to this region. Particles not seeded in locations that can access the potential well formed by the focus ring are, for these conditions, eventually expelled from the bulk plasma.

Typical morphologies of Coulomb crystal lattices, as observed from the top of the reactor through the annular electrode, are shown in Fig. 3. Configurations are shown for low (150 V) and high (250 V) substrate biases. At the lower bias, a single disk-shaped lattice of dust particles, one layer thick, is obtained which is confined to the center of the potential well. Examination of the PCF and Coulomb coupling factor (discussed later) confirm this structure is a Coulomb solid. In the center of the lattice where the confining forces, largely electrostatic and gravitational compressive forces from par-

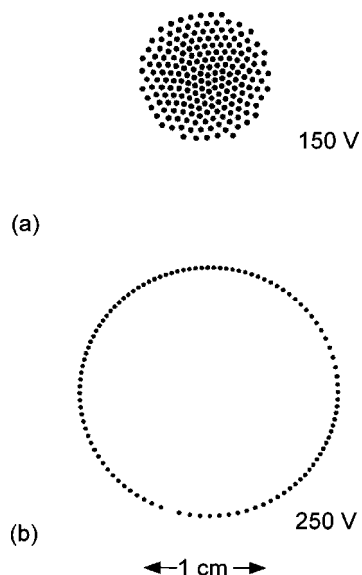


FIG. 3. Top view of particle positions ($4.9 \mu\text{m}$) in an Ar discharge (95 mTorr, 300 sccm). (a) Particles arrange in a central disk for a bias of 150 V. (b) A void is formed at higher biases, shown here for 250 V.

ticles at larger radii, are largest, the lattice has regular hexagonal structure. In the periphery of the lattice where confining forces are smaller, the structure is less regular. The need to match the hexagonal shape of the plasma crystal to a round confining potential causes some defects to appear. As the bias is increased ($>200 \text{ V}$), a void forms in the center of the crystal, resulting in an annular lattice. Voids were created irrespective of the number of initial particles seeded in the system (up to a few hundred), indicating that the formation of the voids is not necessarily a consequence of interparticle forces but rather a consequence of a change in the plasma forces. For example, the radial ion-momentum flux at the level of the particles increased from $2.6 \times 10^{-8} \text{ g/cm}^2 \text{ s}$ for a 150 V bias to $6.6 \times 10^{-8} \text{ g/cm}^2 \text{ s}$ for a 250 V bias. We speculate that larger radial ion-drag forces at higher biases are responsible for the formation of a void as noted by Samsonov and Goree.¹¹ A larger fraction of the initially seeded particles are expelled from the plasma at higher biases as well.

Similar results have been observed experimentally using the apparatus and techniques described in Ref. 6. For this work, the lower electrode with a parabolic shape is replaced by a flat electrode and confinement ring similar to the configuration shown in Fig. 1. For example, particle lattices are shown in Fig. 4 for similar discharge conditions (Ar, 90 mTorr, 20 MHz, $8.34 \mu\text{m}$ particles). At low power (1.8 W), the particles form a single layer, disk-shaped lattice with a hexagonal structure. Upon increasing the rf power (34 W), a void is created in the lattice. The asymmetry in the lattice at higher powers is due to the fact that the surfaces of the electrode and focus rings may not be perfectly leveled and the particles tend to slide down hill or there is azimuthal asymmetry in the plasma.

The influence of particle size on the morphology of Coulomb crystals was investigated by varying the particle radius from 0.1 to $10 \mu\text{m}$ while keeping the number of particles in

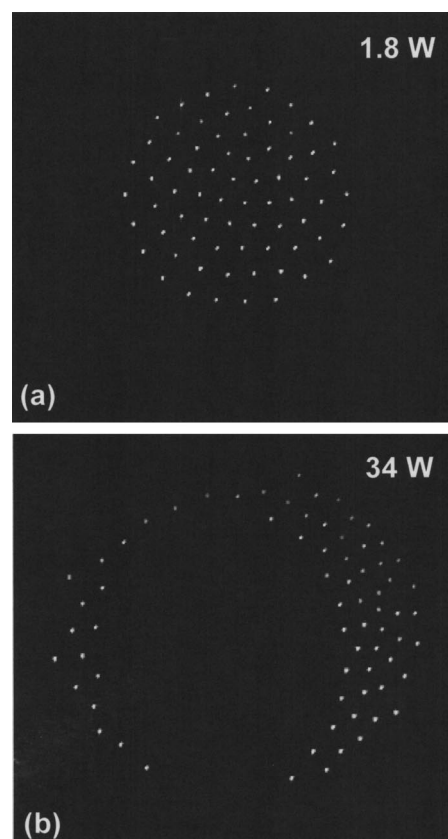


FIG. 4. Experimental results for the evolution of void in a Coulomb crystal for an Ar, 90 mTorr, 20 MHz plasma. (a) 1.8 and (b) 34 W.

the lattice constant at 150. For typical conditions (Ar, 95 mTorr, 150 V), two classes of particle lattices are shown in Fig. 5. We observe two distinct and well-separated structures for smaller particles, such as the $0.1 \mu\text{m}$ particles shown in Fig. 5(a). The upper structure is disk shaped and well above the upper electrode. Particles are trapped at this location due to a balance between the downward pointing electrostatic and upward directed ion-drag forces as gravitational forces are not important for these small particles. Some particles get seeded in the potential well near the bottom electrode and form a ring-shaped structure at a lower location, though at height well above the focus ring. As we increase the size of the particles to $10 \mu\text{m}$ [Fig. 5(b)], the upper lattice disperses as gravitational forces cannot be balanced by the weak ion drag forces in the periphery of the plasma. The $10 \mu\text{m}$ particles arrange themselves in a single disk shaped lattice at a lower height than the smaller particles, a consequence of both their larger mass and larger ion drag forces. There are isolated instances in the edge-on view of Fig. 5(b) where there appear to be two layers to the lattice. The lattice is actually only a single layer. These displaced particles are isolated particles undergoing vertical oscillatory motion, a phenomenon observed by Tomme *et al.*²⁶

As dust particles settle into the potential well forming a Coulomb solid, the resulting lattice often oscillates about an equilibrium position. These radial, horizontal oscillations are the result, in part, of the mutual repulsion of the particles in the presence of a restoring force, in this case both gravity and electrostatic plasma forces. Here the repulsive force is also

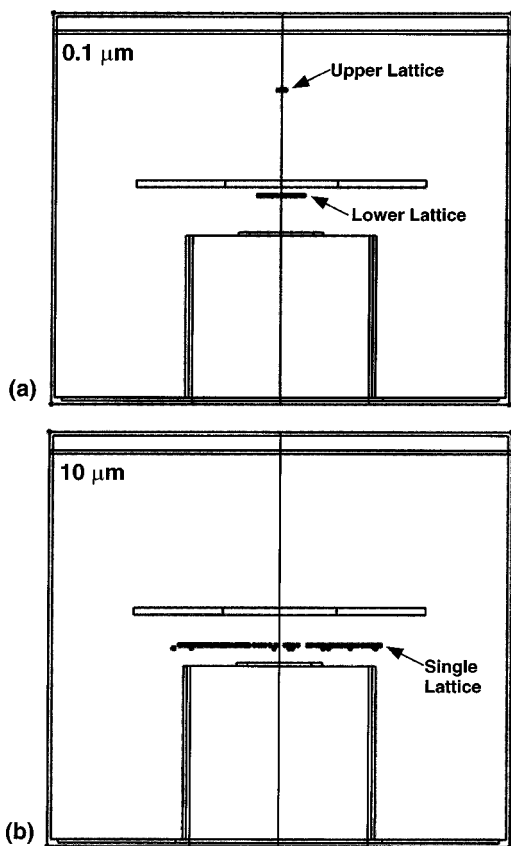


FIG. 5. Effect of particle size on trapping positions in an Ar discharge (95 mTorr, 300 sccm, 150 V). (a) 0.1 μm particles arrange in two lattices; the lower lattice is close to the powered electrode, while the upper lattice is above the upper electrode. (b) 10 μm particles arrange in a single lattice close to the powered electrode.

augmented by a radially outward ion drag force. For typical conditions (Ar, 95 mTorr, 10 W, 4 μm particles), we observe an oscillation frequency of 5 Hz. One complete cycle of such oscillations is shown in Fig. 6. This collective motion is similar to experimentally observed cooperative oscillation also known as a “breathing mode.” For example, Melzer *et al.*²⁷ have observed similar behavior using pulse modulation of the rf electrode voltage to initiate the oscillation. The oscillations observed by Melzer *et al.* damp more quickly than those predicted from our model. Our longer lived oscillations appear to be a result of feedback from the plasma electrostatics which reinforces these largely radial modes.

The consequences of plasma density on interparticle spacing and Coulomb coupling factor were also investigated by artificially increasing ion and electron densities while keeping other conditions constant. Interparticle spacing was determined by the first peak in $g(r)$. The results of this parameterization are summarized in Fig. 7 where Coulomb coupling factor and interparticle spacing are shown as a function of electron density. Recall that above a critical plasma density where the particles do not significantly deplete negative charge in the plasma, the charge on particles is only a function of the electron and ion temperatures. The effect of increasing the plasma density is primarily to change the shielding length. As the plasma density increases, λ_L decreases, thereby reducing the interparticle separation for

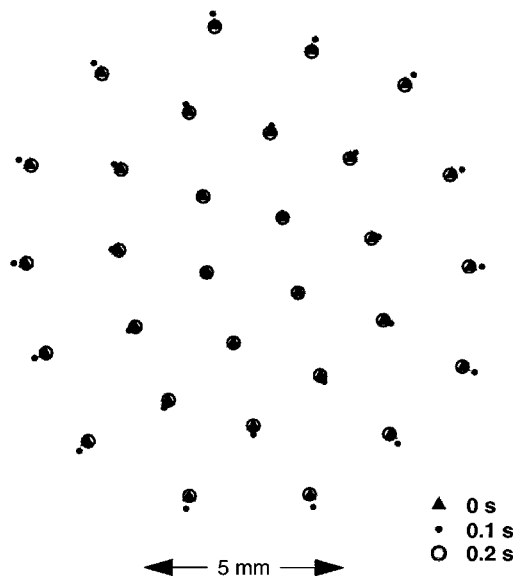


FIG. 6. Horizontal oscillations (5 Hz) of particles in an Ar discharge (95 mTorr, 10 W, 4 μm particles). Particle positions are shown at different times during one complete cycle. Cooperative oscillation of particles such as this are often referred to as a breathing mode.

which a given force is experienced. The end result is a decrease in interparticle spacing. More aggressive shielding produces less electrostatic interaction and a decrease in the Coulomb coupling factor. The exception is at low plasma densities where the interparticle spacing increases because of

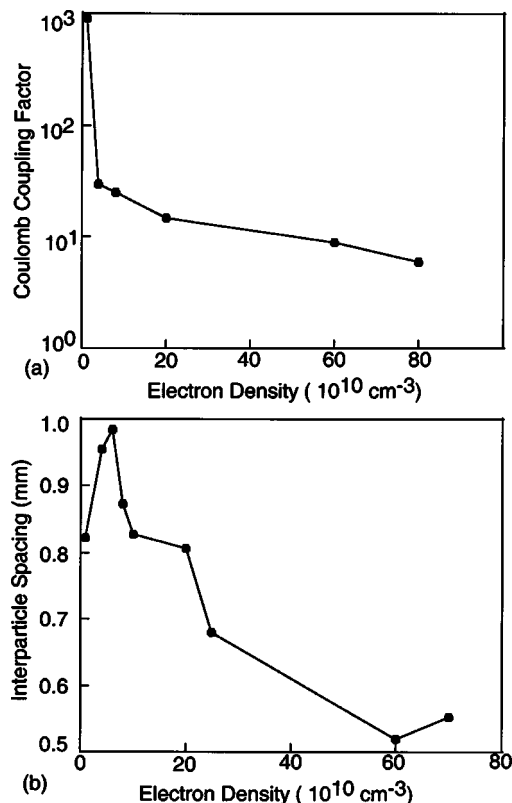


FIG. 7. Effect of plasma density on the (a) Coulomb coupling factor and (b) interparticle spacing. Ion and electron densities were varied keeping other conditions constant in an Ar discharge (95 mTorr, 300 sccm, 150 V).

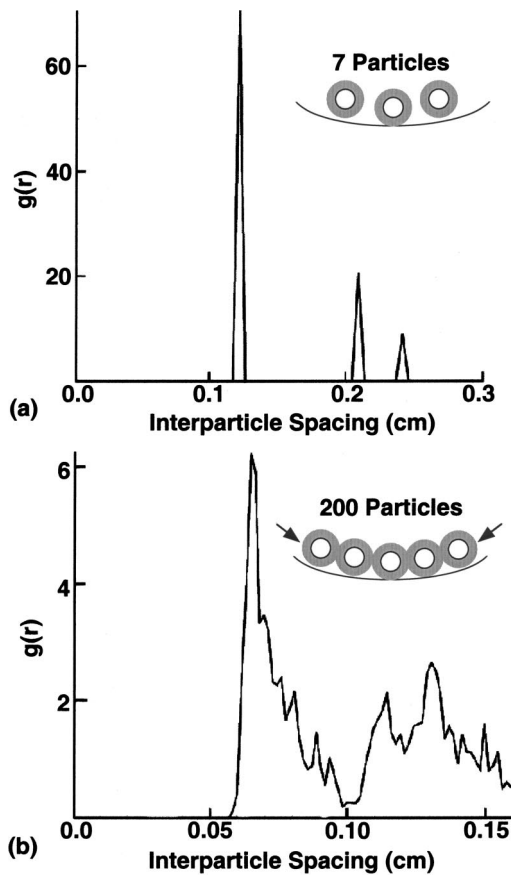


FIG. 8. Effect of particle number on PCF in an Ar discharge (95 mTorr, 300 sccm, 150 V, 3.8 μm particles). (a) 7 particles and (b) 200 particles. The first nearest neighbor peak is shifted to lower values on increasing the number of particles. The inset schematics illustrate the consequences of increasing the number of particles on the inward radial force.

an increase in the particle temperature. This increase in particle temperature is responsible for the large initial drop in the Coulomb coupling factor, which then more slowly decreases commensurate with the decrease in shielding length.

The consequences of the number of particles on interparticle spacing was also investigated. The first, nearest neighbor peak of $g(r)$ was used to determine the average particle separation. $g(r)$ for base case conditions are shown in Fig. 8 for lattices having 7 and 200 particles. Top views of these lattices, and for 500 particles, are shown in Fig. 9. Computed interparticle separations for 3.8 μm particles as a function of the number of particles in the lattice are shown in Fig. 10(a), and result for similar experimental conditions are shown Fig. 10(b). Increasing the number of particles in the lattice generally decreases the interparticle spacing, as more particles accessing a finite-sized potential well leads to radial compression of the plasma crystal. $g(r)$ for the smaller crystal has well defined peaks due to the near perfect hexagonal arrangement of the particles. $g(r)$ for the larger crystal has less well defined peaks due to the propensity for dislocations and the fact that the particle spacing is a function of radius in the crystal. For example, nearest neighbor spacing as a function of radial position for a plasma crystal containing 200 particles is shown in Fig. 10(c). The nearest neighbor spacing is smallest in the center of the crystal where the com-

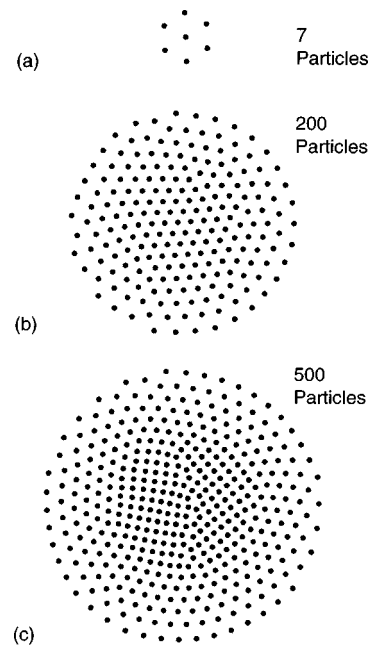


FIG. 9. Top views of the particle crystal for (a) 7 particles, (b) 200 particles, and (c) 500 particles. Interparticle spacing is smaller in the center of the larger crystals due to compressive forces from particles at larger radii.

pressive forces of particles at larger radii are the largest, and these forces add to the radial plasma forces which provide the overall confinement for the lattice. As one moves to larger radii, the compressive forces due to outlying particles lessens, leaving only the plasma confining forces, producing a larger interparticle separation. Similar results have been reported by Hebner *et al.*^{6,28,29} The Coulomb coupling factor increases with an increase in the number of particles due to the decrease in interparticle spacing and a decrease in the particle temperature, as shown in Fig. 11.

There is no clear correlation between the substrate bias and the interparticle spacing as several competing effects come into play. An increase in bias leads to higher plasma densities and so a reduced shielding length should produce smaller interparticle spacing. However, particle temperatures tend to be larger at higher biases and that effect should produce larger interparticle spacings. The interparticle spacing decreased with an increase in the number of particles for all biases we examined, however, for a fixed number of particles the trend was not monotonic with increasing bias.

IV. COULOMB CRYSTALS IN ELECTRONEGATIVE PLASMAS

The morphology of Coulomb crystals in electronegative plasmas has been the focus of recent investigations.³⁰ The negative ion density in an electronegative plasma can often greatly exceed the electron density. As a consequence, the ion drag force acting on the dust particles and the charge on particles can be different, leading to qualitatively different crystal morphologies than those found in electropositive plasmas. To investigate the effect of negative ions on crystal morphologies, O_2 and Cl_2 were added to Ar in various proportions. For example, crystal morphologies for pure argon and $\text{Ar}/\text{Cl}_2 = 90/10$ are compared in Fig. 12. For pure Ar, the

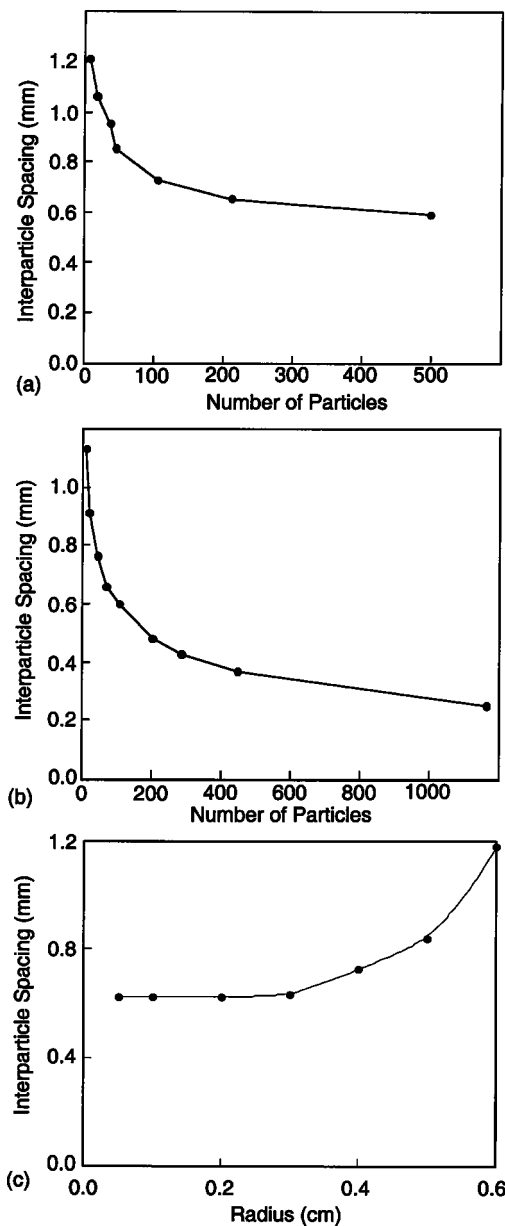


FIG. 10. Interparticle spacing for $3.8 \mu\text{m}$ particles (Ar, 95 mTorr, 300 sccm). (a) Computed distances as a function of the number of particles in the lattice, (b) experimentally observed interparticle spacing in an Ar, 110 mTorr, 1.8 W plasma (see Ref. 6), and (c) computed nearest neighbor separation as a function of radial position for Coulomb crystal containing 200 particles.

particles settle in a ring-shaped configuration. On increasing the Cl_2 fraction to 0.1, the void closes and the particles settle into a single, small disk-shaped structure. More particles are also lost from the plasma.

The cause for this behavior is ultimately rooted in the electron density and ion momentum flux vectors, as shown in Fig. 13. The peak electron density in the reactor decreased from $3 \times 10^{10} \text{ cm}^{-3}$ for Ar to $6 \times 10^8 \text{ cm}^{-3}$ for $\text{Ar}/\text{Cl}_2 = 90/10$ while the ion density remains roughly constant. The resulting increase in the sheath thickness in the electronegative plasma decreased the peak electrostatic fields in the sheath from 280 V/cm for pure Ar to 145 V/cm for $\text{Ar}/\text{Cl}_2 = 90/10$. The charge on the dust particles is smaller in the

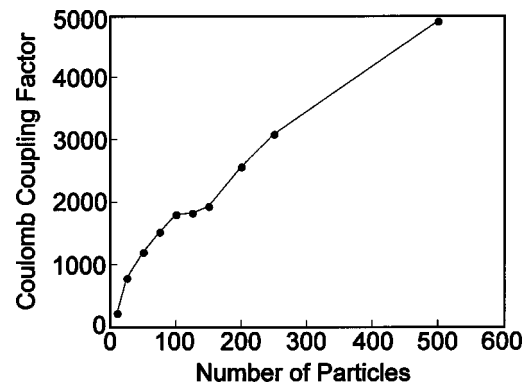


FIG. 11. Coulomb coupling factor as a function of the number of particles in an Ar discharge (95 mTorr, 300 sccm, 150 V).

electronegative mixture due to the increase in the positive ion flux relative to the electron flux. The reduction in charge combined with the smaller electric fields in the sheath leads to reduced electrostatic shielding and larger propensity for particles not to be trapped. The shape of the crystals is dominantly a function of a change in the direction of the ion momentum flux. The mass averaged ion momentum flux exerts an outward ion drag on the particles in pure Ar which leads to the formation of a void [see Fig. 13(a)] whereas in Ar/Cl_2 plasmas, the net ion-momentum flux pushes particles to the center of the reactor and causes the void to close [see Fig. 13(b)].

A similar result is observed in Ar/O_2 for oxygen fractions of 0.0–0.6. The reduction in electron density on increasing the oxygen fraction is less than for Ar/Cl_2 plasmas as oxygen is a less electronegative gas than chlorine. For example, the peak electron density varied from $3.5 \times 10^9 \text{ cm}^{-3}$ for $\text{Ar}/\text{O}_2 = 80/20$ to $1 \times 10^9 \text{ cm}^{-3}$ for $\text{Ar}/\text{O}_2 = 40/60$.

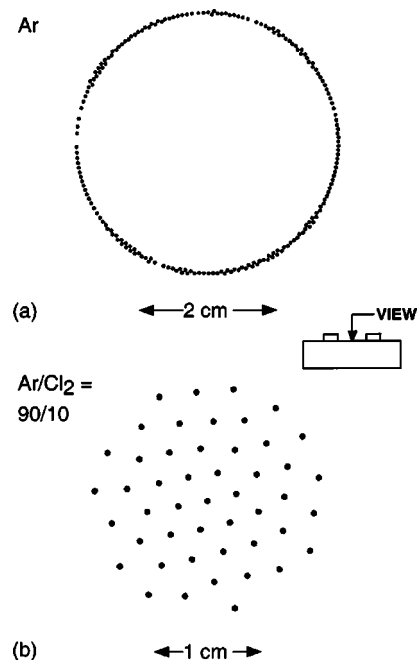


FIG. 12. Plasma crystal morphologies in an Ar/Cl_2 discharge (14 sccm, 0.14 Torr, 40W). (a) Pure Ar. (b) $\text{Ar}/\text{Cl}_2 = 90/10$. Addition of Cl_2 causes the plasma void to close.

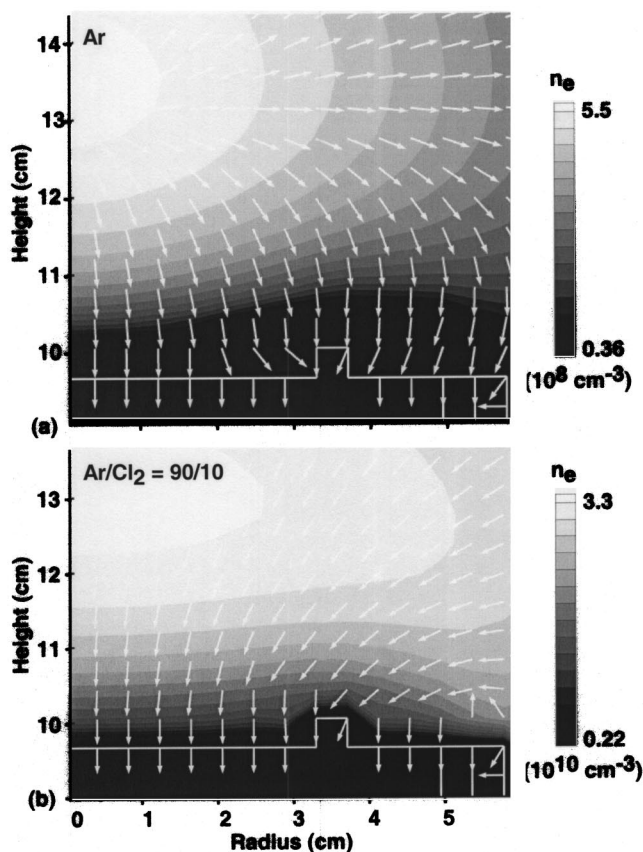


FIG. 13. Electron density and ion-momentum-flux vectors in rf discharge (14 sccm, 0.14 Torr, 40W). (a) Pure Ar and (b) Ar/Cl₂=90/10. The reorientation of the ion momentum flux vectors upon addition of electronegative gas causes the void to close.

The resulting plasma crystal morphologies for these cases are shown in Fig. 14. Whereas in Ar/Cl₂ the ring structure collapsed to a disk with only 10% admixture of Cl₂, the ring structure in Ar/O₂ is maintained to mole fractions exceeding 50%. With sufficient Ar/O₂ addition, the ion momentum flux eventually transitions from being radially outward to radially inward, and the crystal morphology transitions from a ring to a disk. These results are in agreement with experimentally observed trends.³⁰

V. CONCLUDING REMARKS

A self-consistent three-dimensional model has been developed to investigate particle transport and Coulomb crystal formation in plasma processing reactors. The propensity for crystal formation as a function of various process parameters such as substrate bias, gas chemistries, particle size, and number were discussed. In particular, we found that the Coulomb crystal typically contained a void at high substrate biases and low electronegativities due to larger radial ion-drag forces. These ring-like structures collapsed to a disk upon addition of electronegative gases, commensurate with a shift in the net ion momentum flux vectors to having a radially inward component. The interparticle spacing decreases on increasing the number of particles in the lattice due to larger compressive forces from particles at larger radii.

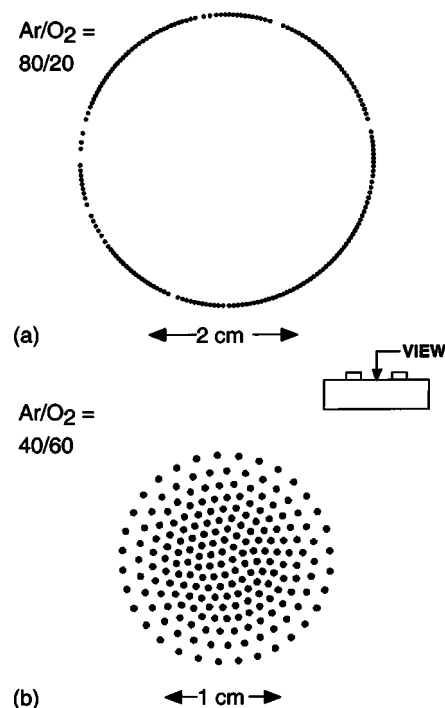


FIG. 14. Plasma crystal morphologies in an Ar/O₂ discharge (14 sccm, 0.14 Torr, 40W). (a) Ar/O₂ = 80/20 wherein a void is formed in the plasma crystal because of the larger ion-drag forces. (b) Ar/O₂ = 40/60 wherein the void in the plasma crystal closes.

ACKNOWLEDGMENTS

This work is supported by the Division of Material Sciences, Basic Energy Sciences, U.S. Department of Energy and Sandia National Laboratories, No. (DE-AC04-94AL85000), the National Science Foundation No. (CTS99-74962), and the Semiconductor Research Corporation.

- ¹M. Roth, K. G. Spears, G. D. Stein, and G. Wong, *Appl. Phys. Lett.* **46**, 235 (1985).
- ²L. Boufendi, A. Bouchoule, R. K. Porteous, J. Ph. Blondeau, A. Plain, and C. Laure, *J. Appl. Phys.* **73**, 2160 (1993).
- ³J. H. Chu, J.-B. Du, and I. Lin, *J. Phys. D* **27**, 296 (1994).
- ⁴H. Thomas, G. E. Morfill, V. Demmel, J. Goree, B. Feuerbacher, and D. Möhlmann, *Phys. Rev. Lett.* **73**, 652 (1994).
- ⁵Th. Trottenberg, A. Melzer, and A. Piel, *Plasma Sources Sci. Technol.* **4**, 450 (1995).
- ⁶G. A. Hebner, M. E. Riley, D. S. Johnson, P. Ho, and R. J. Buss, *Phys. Rev. Lett.* **87**, 235001 (2001).
- ⁷J. B. Pieper, J. Goree, and R. A. Quinn, *J. Vac. Sci. Technol. A* **14**, 519 (1996).
- ⁸A. Melzer, A. Homann, and A. Piel, *Phys. Rev. E* **53**, 2757 (1996).
- ⁹G. Joyce, M. Lampe, and G. Ganguli, *IEEE Trans. Plasma Sci.* **29**, 238 (2001).
- ¹⁰Collection of papers on particles in plasmas can be found in the following special issues: *IEEE Trans. Plasma Sci.* **29**, 146–312 (2001); **3**, 91–186 (1994).
- ¹¹D. Samsonov and J. Goree, *Phys. Rev. E* **59**, 1047 (1999).
- ¹²T. Nitter, T. K. Aslaksen, F. Melandsoi, and O. Havnes, *IEEE Trans. Plasma Sci.* **22**, 159 (1994).
- ¹³T. Nitter, *Plasma Sources Sci. Technol.* **5**, 93 (1996).
- ¹⁴M. Zuzic, H. M. Thomas, and G. E. Morfill, *J. Vac. Sci. Technol. A* **14**, 496 (1996).
- ¹⁵G. E. Morfill, H. M. Thomas, and M. Zuzic, in *Advances in Dusty Plasmas*, edited by P. K. Shukla, D. A. Mendis, and T. Desai (World Scientific, Singapore, 1997), pp. 99–142.

- ¹⁶F. Melandso, *Phys. Plasmas* **3**, 3890 (1996).
- ¹⁷W. Z. Collison and M. J. Kushner, *Appl. Phys. Lett.* **68**, 903 (1996).
- ¹⁸R. L. Kinder and M. J. Kushner, *J. Vac. Sci. Technol. A* **19**, 76 (2001).
- ¹⁹H. H. Hwang and M. J. Kushner, *J. Appl. Phys.* **82**, 2106 (1997).
- ²⁰J. E. Daugherty, R. K. Porteous, M. D. Kilgore, and D. B. Graves, *J. Appl. Phys.* **72**, 3934 (1992).
- ²¹M. D. Kilgore, J. E. Daugherty, R. K. Porteous, and D. B. Graves, *J. Appl. Phys.* **73**, 7195 (1993).
- ²²S. A. Khrapak, A. V. Ivlev, G. E. Morfill, and H. M. Thomas, *3rd International Conference on the Physics of Dusty Plasmas*, Durban, 2002.
- ²³S. J. Choi and M. J. Kushner, *IEEE Trans. Plasma Sci.* **22**, 138 (1994).
- ²⁴M. Mitchner and C. H. Kruger, *Partially Ionized Gases* (Wiley, New York, 1973).
- ²⁵R. A. Quinn, C. Cui, J. Goree, J. B. Pieper, H. Thomas, and G. E. Morfill, *Phys. Rev. E* **53**, R2049 (1996).
- ²⁶E. B. Tomme, B. M. Annaratone, and J. E. Allen, *Plasma Sources Sci. Technol.* **9**, 87 (2000).
- ²⁷A. Melzer, M. Klindworth, and A. Piel, *Phys. Rev. Lett.* **87**, 115002 (2001).
- ²⁸G. A. Hebner, M. E. Riley, D. S. Johnson, P. Ho, and R. J. Buss, *IEEE Trans. Plasma Sci.* **30**, 94 (2002).
- ²⁹G. A. Hebner, M. E. Riley, and K. E. Greenberg, *Phys. Rev. E* (to be published).
- ³⁰R. P. Dahiya, G. Paeva, W. W. Stoffels, E. Stoffels, and G. M. W. Kroesen, *54th Gaseous Electronics Conference*, Pennsylvania State University, 2001.